

# Interplay of electron correlations, spin-orbit couplings, and structural effects for Cu centers in the quasi-two-dimensional magnet $\text{InCu}_{2/3}\text{V}_{1/3}\text{O}_3$

R. Murugesan,<sup>1</sup> M. S. Eldeeb,<sup>1</sup> M. Yehia,<sup>1,2</sup> B. Büchner,<sup>1,3</sup> V. Kataev,<sup>1</sup> O. Janson,<sup>1</sup> and L. Hozoi<sup>1</sup>

<sup>1</sup>*Leibniz IFW Dresden, Helmholtzstr. 20, 01069 Dresden, Germany*

<sup>2</sup>*Reactor Physics Department, Nuclear Research Center, Atomic Energy Authority, Cairo, Egypt*

<sup>3</sup>*Institute for Solid State and Materials Physics and Würzburg-Dresden*

*Cluster of Excellence ct.qmat, TU Dresden, D-01062 Dresden, Germany*

(Dated: February 9, 2022)

Less common ligand coordination of transition-metal centers is often associated with peculiar valence-shell electron configurations and outstanding physical properties. One example is the  $\text{Fe}^+$  ion with linear coordination, actively investigated in the research area of single-molecule magnetism. Here we address the nature of  $3d^9$  states for  $\text{Cu}^{2+}$  ions sitting in the center of trigonal bipyramidal ligand cages in the quasi-two-dimensional honeycomb compound  $\text{InCu}_{2/3}\text{V}_{1/3}\text{O}_3$ , whose unusual magnetic properties were intensively studied in the recent past. In particular, we discuss the interplay of structural effects, electron correlations, and spin-orbit couplings in this material. A relevant computational finding is a different sequence of the Cu ( $xz, yz$ ) and ( $xy, x^2 - y^2$ ) levels as compared to existing electronic-structure models, which has implications for the interpretation of various excitation spectra. Spin-orbit interactions, both first- and second-order, turn out to be stronger than previously assumed, suggesting that rather rich single-ion magnetic properties can be in principle achieved also for the  $3d^9$  configuration by properly adjusting the sequence of crystal-field states for such less usual ligand coordination.

## I. Introduction

Transition-metal (TM) ions with atypical ligand (L) coordination in TM pnictides, chalcogenides, and halides may display quite unexpected features as concerns their electronic structures and physical properties. A remarkable example is monovalent Fe with linear L-Fe-L bonds, which due to its impressively strong magnetic anisotropy is being presently investigated in the context of single-molecule magnetism [1, 2]. Also rare is for instance the square coordination realized for nickel (formally  $3d^9$ ) in  $\text{NdNiO}_2$ . Interestingly, superconductivity with  $T_c$ 's of up to 15 K was recently reported in this system [3], the available data suggesting physics significantly different as compared to the Cu-oxide superconductors [4, 5].

The title compound of the present study, honeycomb  $\text{InCu}_{2/3}\text{V}_{1/3}\text{O}_3$ , has attracted significant attention due to its peculiar magnetic properties [6–12]. In particular, it has been found recently [13] that a pronounced two-dimensional (2D)  $XY$  anisotropy of the Cu-based honeycomb spin-1/2 planes and strong inter-layer frustration yield an extended low-temperature regime where a quasi-2D static magnetic state is stabilized, showing some indications of a Berezinsky-Kosterlitz-Thouless transition to the topologically ordered state of vortex-antivortex pairs predicted in the 2D  $XY$  model [14–17]. An interesting aspect is the uncommon type of ligand environment encountered in this compound, with trigonal ligand bipyramids around each copper ion. For  $D_{3h}$  Cu-site symmetry as realized in this situation, there are two sets of doubly degenerate orbitals ( $xz, yz$  and  $xy, x^2 - y^2$ ), as for magnetically anisotropic L-TM-L units with either  $D_{6h}$  [2, 18–20] or approximate  $D_{3h}$  [1] symmetry. Finding that spin-orbit (SO) interactions play an important role for such hole configurations in various L-TM-L complexes

motivates then a detailed investigation of SO interactions for Cu  $3d^9$  hole states in  $\text{InCu}_{2/3}\text{V}_{1/3}\text{O}_3$ . Even if the  $z^2$  ground-state character inferred from analysis of electron spin resonance (ESR) spectra [6] and by band-structure calculations [13, 21] indicates that to first order only the excited states would be affected by SO couplings in this particular cuprate, such a study should still provide insights into the prospect of strong single-ion magnetic anisotropy for  $3d^9$  centers with suitably engineered environments in related systems. In addition to first-order SO interactions, here we also analyze in detail second-order effects, in particular, their impact on the ground-state  $g$  factors and on the structure of the on-site excitation spectrum.

## II. Ground-state $g$ factors, experiment vs *ab initio* computations

Within the family of layered Cu-oxide compounds, the type of  $g$ -factor anisotropy featured by Cu centers in  $\text{InCu}_{2/3}\text{V}_{1/3}\text{O}_3$ ,  $g_{ab} > g_c$ , is unusual since for the large majority of cuprates  $g_{ab} < g_c$  is commonly found ( $g_{ab}$  and  $g_c$  are here the in-plane and out-of-plane components of the  $\mathbf{g}$  tensor, respectively). This aspect was first noticed in Ref. [6], confirmed in Ref. [9], and attributed to a less common ground-state configuration having one hole in the  $z^2$  Cu  $3d$  orbital. To better substantiate these earlier findings and interpretations, we perform in this work detailed electronic-structure calculations for this material. To illustrate and further document the experimental basis and to facilitate the discussion of the computational results we first present additional ESR data measured on a powder sample of  $\text{InCu}_{2/3}\text{V}_{1/3}\text{O}_3$ , synthesized and thoroughly characterized in Ref. [7]. The powder was

mixed with an epoxy resin and the mixture was hardened in a magnetic field of several Tesla. As a result, the so-prepared sample acquired a well-defined anisotropy axis (referred to hereafter as orientation  $o$  axis) [6] which according to x-ray diffraction measurements is perpendicular to the crystallographic  $c$  axis.

The dependence of the  $g$  factor  $g = h\nu/\mu_B\mu_0H_{\text{res}}$  and of the ESR peak-to-peak linewidth  $\Delta H_{\text{pp}}$  on the angle  $\alpha$  which the applied magnetic field  $\mathbf{H}$  makes with the  $o$  axis are shown in Fig. 1, as measured with a commercial X-band Bruker spectrometer at a frequency  $\nu = 9.59$  GHz and room temperature.  $h$ ,  $\mu_B$ , and  $\mu_0$  are here the Planck constant, the Bohr magneton, and the vacuum permeability, respectively. The parameters of the ESR signal  $H_{\text{res}}$  (resonance field) and  $\Delta H_{\text{pp}}$  are defined in the inset of Fig. 1. The  $g$  factor for  $\alpha = 0$  corresponds to the single-crystalline in-plane  $g$  factor  $g_{ab}$ , whereas for  $\alpha = \pm 90^\circ$  it yields the powder averaged  $g$  factor  $g_{\text{pow}}$ . To model the experimental dependence of  $g$  and  $\Delta H_{\text{pp}}$  on  $\alpha$  we performed numerical simulations of the ESR signal which account for the  $\alpha$ -dependent averaging of the contributions from the individual crystallites in the sample. The  $g(\alpha)$  dependence can be very well reproduced, yielding the single-crystalline  $g$  values  $g_c = 2.020 \pm 0.015$

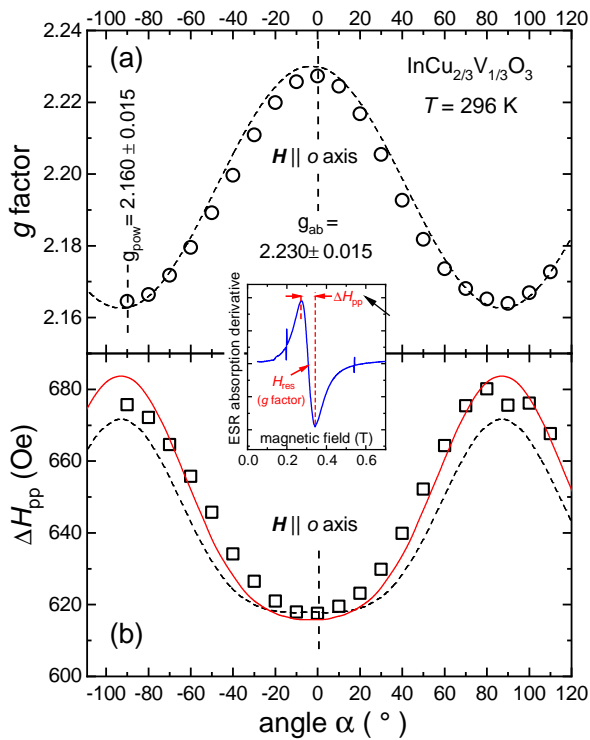


FIG. 1. Angular dependence of the  $g$  factor (a) and of the peak-to-peak ESR linewidth  $\Delta H_{\text{pp}}$  (b) of the oriented powder sample of  $\text{InCu}_{2/3}\text{V}_{1/3}\text{O}_3$  measured at room temperature at the X-band frequency  $\nu = 9.58$  GHz (symbols). The inset shows a typical ESR signal (field derivative of the microwave absorption). Dashed and solid curves are the results of numerical modeling (see main text).

and  $g_{ab} = 2.230 \pm 0.015$  [dashed line in Fig. 1(a)]. The  $g$ -factor anisotropy should give rise to a dependence of the measured peak-to-peak linewidth  $\Delta H_{\text{pp}}$  on the angle  $\alpha$ . For  $\alpha = 0$ , the ESR signal has the width corresponding to the single-crystalline line  $\Delta H$ ,  $\Delta H_{\text{pp}}(\alpha = 0) = \Delta H$ . For  $\alpha = \pm 90^\circ$ , the ESR linewidth  $\Delta H_{\text{pp}}(\alpha = \pm 90^\circ)$  corresponds to that of the powder sample and should be larger because of the distribution of the resonance fields of the individual crystallites arising from the  $g$ -factor anisotropy,  $\Delta H_{\text{pp}}(\alpha = \pm 90^\circ) > \Delta H$ . However, the respective  $\Delta H_{\text{pp}}(\alpha)$  modeled curve noticeably deviates from experiment [dashed line in Fig. 1(b)], indicating that the  $\Delta H_{\text{pp}}(\alpha)$  dependence is not entirely due to averaging signals with anisotropic  $g$  factors. Therefore, in addition, one could also consider a possible angular dependence of the width of individual single-crystalline ESR lines of the form  $\Delta H = A + B \cdot (1 + \cos^2 \theta)$ , where  $\theta$  denotes the angle between  $\mathbf{H}$  and the  $c$  axis. Here, the first term is the linewidth in the absence of spin correlations at  $T \rightarrow \infty$  and the second term is the angular dependent contribution due to the three-dimensional (3D) antiferromagnetic correlations at finite temperature [22–26]. Indeed, accounting for this additional contribution in the simulation, with  $A = 571$  Oe and  $B = 45$  Oe, significantly improves the agreement with the experiment [solid line in Fig. 1(b)]. The 3D-like behavior of  $\text{InCu}_{2/3}\text{V}_{1/3}\text{O}_3$  at elevated temperature is not surprising since the in-plane spin correlations turning this compound into a 2D- $XY$  magnet begin to grow at temperatures  $\lesssim 50$  K [13].

Finally, a more accurate value can be obtained for  $g_{ab}$  from the frequency  $\nu$  versus field  $H$  dependence of the ESR signal, which we measured using the home-made high-field ESR setup described in [8] at a lower temperature  $T = 60$  K (Fig. 2). A fit of the data to the resonance condition  $\nu = g_{ab}\mu_B\mu_0H/h$  yields  $g_{ab} = 2.25 \pm 0.01$ . With  $g_{\text{pow}} = 2.23$ , one obtains from the relation  $g_{\text{pow}} = (1/3)g_c + (2/3)g_{ab}$  [6] the  $c$ -axis  $g$  factor  $g_c = 1.99$ . The resulting  $\mathbf{g}$  tensor  $(g_{ab}, g_c) = (2.25, 1.99)$  is, within error bars of  $\pm 5$ –10%, fully consistent with values obtained for other samples of  $\text{InCu}_{2/3}\text{V}_{1/3}\text{O}_3$  from various sources and for batches earlier studied in Refs. [6, 9], providing altogether a solid reference for theoretical analysis.

Two complementary computational techniques were employed for addressing the Cu  $3d$ -shell electronic structure in  $\text{InCu}_{2/3}\text{V}_{1/3}\text{O}_3$  and peculiar features such as the  $g_{ab} > g_c$  anisotropy of the  $g$  factor. In a first step we determined the optimal atomic positions in the frame of density-functional calculations with periodic boundary conditions. We used to this end the full-potential local-orbital code FPLO, version 18 [27]. For nonmagnetic scalar-relativistic as well as fully relativistic computations, we utilized the generalized gradient approximation (GGA) [28]. A  $k$ -mesh of  $14 \times 14 \times 7$  points was employed in either case. Typical for undoped cuprates, GGA yields a spurious metallic state in  $\text{InCu}_{2/3}\text{V}_{1/3}\text{O}_3$ . This well-known artifact stems from underestimating electronic correlations with conventional functionals such as GGA. The insulating state can be restored in DFT++

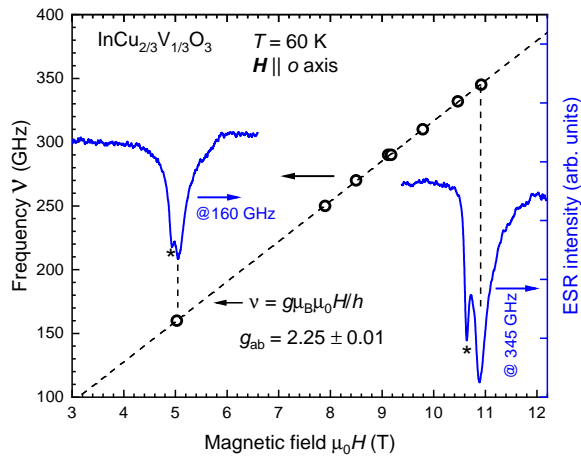


FIG. 2. Frequency  $\nu$  versus magnetic field  $H$  dependence of the ESR signal of the oriented powder sample of  $\text{InCu}_{2/3}\text{V}_{1/3}\text{O}_3$  measured at  $T = 60$  K with  $\mathbf{H} \parallel \mathbf{o}$  axis (open circles). A corresponding fit is shown as dashed line. Exemplary ESR signals are shown for frequencies of 160 and 345 GHz. The asterisk labels a small additional peak presumably due to  $\text{Cu}^{2+}$  spins at defect sites.

approaches, where interactions are considered explicitly on the level of (extended) multi-orbital Hubbard models [29]. Nevertheless, the non-interacting part of such models is adopted from conventional DFT calculations. Hence, the respective model parameters, transfer integrals and crystal-field splittings, are not affected by shortcomings of the GGA.

$\text{InCu}_{2/3}\text{V}_{1/3}\text{O}_3$  is a quasi-2D material whose honeycomb planes are only weakly coupled to each other. All samples synthesized so far feature a sizable number of stacking faults, impeding a complete characterization of the crystal structure [7]. Hence, the first step of our computational analysis was the construction of a 3D structural model, based on the experimentally available information: lattice constants and the internal coordinates of a single honeycomb plane with Cu and V occupying the same crystallographic site [7]. As explained in Ref. [13], a minimal 3D structural model for  $\text{InCu}_{2/3}\text{V}_{1/3}\text{O}_3$  employs the orthorhombic space group  $Cmcm$  (63), which is compatible with a fully ordered honeycomb lattice of Cu atoms and at the same time supports the simplest type of stacking of the honeycomb planes. The respective atomic coordinates are provided in Table I. The Cu-site point group symmetry is in this space group  $C_s$  instead of  $D_{3h}$ .

The parent structural model [7] does not distinguish between Cu and V, featuring identical  $\text{O}_5$  cages around Cu and V atoms. However, the honeycomb planes in  $\text{InCu}_{2/3}\text{V}_{1/3}\text{O}_3$  may undergo a breathing distortion, giving rise to unequal Cu-O and V-O bond lengths. To address this possibility, we performed a structural relaxation of O positions within the space group  $P2_1/m$ , supporting Néel antiferromagnetic order. To avoid inaccuracies stemming from the spurious metallic ground

TABLE I. Atomic sites, Wyckoff positions (Wyck. pos.), and internal coordinates of the two different crystal structures used in this study. The space group is  $Cmcm$  (63), with  $a = 10.0527$ ,  $b = 5.80393$ ,  $c = 11.9012$  Å. In the computationally optimized structure, the O positions were relaxed within the antiferromagnetic (Néel) structure to yield the lowest total energy at the GGA+ $U$  level.

Site	Wyck. pos.	Identical $\text{O}_5$ cages			Optimized O positions		
		$x/a$	$y/b$	$z/c$	$x/a$	$y/b$	$z/c$
Cu	8g	$1/3$	$1/3$	0.25			
V	4c	0	$1/3$	0.25			
In1	4a	0	0	0			
In2	8e	$2/3$	0	0			
O1	4c	0	0	0.25	0	0.03400	0.25
O2	8g	$1/3$	0	0.25	0.35045	0.98309	0.25
O3	8f	0	$2/3$	0.5864	0	0.66708	0.58500
O4	16h	$1/3$	$1/3$	0.0864	0.33313	0.33359	0.09067

state, the optimization was carried out with respect to the GGA+ $U$  energy. Following earlier studies on low-dimensional cuprates [30, 31], we use a Coulomb repulsion parameter  $U = 8.5$  eV, a Hund's exchange  $J = 1$  eV, and the fully localized limit for the double-counting correction. We find this way large differences between the in-plane Cu-O and V-O bond lengths, 2.04 vs 1.74 Å, consistent with considerations concerning the difference between the formal oxidation states of copper and vanadium in this system [7]. Also, the computationally derived lattice parameters imply significantly longer in-plane Cu-O links as compared to the apical Cu-O bonds (2.04 vs 1.90 Å).

Using crystallographic data as listed in Table I, we further performed many-body quantum chemical calculations [32] on a finite atomic fragment having a  $\text{CuO}_5$  unit as central region (all relevant computational details are provided in Appendix). To describe configurational mixing effects mediated by SO interactions and related  $g$ -factor anisotropies we relied on spin-orbit multiconfiguration and multireference numerical schemes as implemented in the quantum chemical package MOLPRO [33] by Berning *et al.* [34]. An active space defined by the Cu 3d orbitals (nine electrons in five orbitals) was used to this end in preliminary multiconfiguration computations [32]. All possible states associated with this 3d-shell filling were considered, which in quantum chemical terminology is referred to as complete-active-space self-consistent-field (CASSCF) methodology [35]. The  $z^2$  character of the Cu 3d hole proposed on the basis of the measured  $g_{ab} > g_c$  structure of the  $g$  factors [6] is also confirmed in the CASSCF calculation. For making direct connection with the experimental data,  $g$  factors were also computed: using CASSCF wave-functions, related angular-momentum and SO matrix elements [34], and the methodology described in Ref. [36], we arrive to  $g_{ab} = 2.23$  and  $g_c = 1.96$ ; on the basis of multireference configuration-interaction (MRCI) wave-functions built by additionally considering single and double exci-

tations [37] out of the Cu  $3d$  and O  $2p$  orbitals of the  $\text{CuO}_5$  polyhedron, we obtain  $g_{ab} = 2.21$  and  $g_c = 1.97$ . These CASSCF and MRCI values are within 98–99% of the estimates derived from the ESR data and presented above. For a more detailed picture on the Cu  $3d$ -shell electronic structure in this compound, we analyze in the following the Cu  $d$ - $d$  excitations since the  $g$ -factor values depend on the relative energies of the excited states.

### III. Excited states

CASSCF, MRCI, and spin-orbit MRCI (SO-MRCI) results for the  $\text{Cu}^{2+}$  multiplet structure using atomic positions as determined by density-functional lattice optimization are listed in Table II. Notations corresponding to  $D_{3h}$  point-group symmetry are employed, where the Cu  $z^2$ ,  $(xy, x^2 - y^2)$ , and  $(xz, yz)$  orbitals belong to the irreducible representations  $A'_1$ ,  $E'$ , and  $E''$ , respectively. It is found that the two sets of doubly degenerate levels lie rather close in energy and that the MRCI treatment brings corrections of 0.1–0.2 eV to the CASSCF crystal-field splittings. Rectifications in this range were previously computed at the MRCI level in other copper oxide compounds [38, 39] and mainly originate from L  $2p$ –TM  $3d$  charge-transfer-type correlation effects. SO interactions lift the degeneracy of the  $E'$  and  $E''$  states and additionally lead to some degree of  $E' - E''$  mixing. This is an aspect that deserves attention: since  $A'_1$  to  $E''$  dipole transitions are not allowed, the three-peak structure of the optical absorption spectrum [7] can be then qualitatively understood on the basis of the fact that only three of the four SO excited states have significant  $E'$  character (see the right column in Table II).

The  $E' - E''$  mixing is obviously the effect of second-order SO couplings. Such physics was not addressed in detail in earlier analysis of the Cu  $d$ - $d$  excitation spectrum of  $\text{InCu}_{2/3}\text{V}_{1/3}\text{O}_3$  but given the near-degeneracy of the  $E'$  and  $E''$  crystal-field-like states it plays a significant role. To better illustrate this point, we performed SO calculations for each of the  $E'$  and  $E''$  terms separately. The splittings induced by first-order SO interactions came out as 200 meV and 101 meV, respectively. Taking as reference the MRCI relative energies provided

TABLE II.  $\text{Cu}^{2+} 3d^9$  multiplet structure (relative energies in eV) using atomic positions as obtained by density-functional optimization. The MRCI values include Davidson corrections [32]. The character of the SO wave-functions is also specified.

$3d^9$ states	CASSCF	MRCI	SO-MRCI
${}^2A'_1$	0	0	0 (99% $A'_1$ character)
${}^2E''$	1.03	1.20	1.12 (89% $E''$ , 11% $E'$ ) 1.21 (99% $E'$ )
${}^2E'$	1.12	1.30	1.28 (99% $E''$ ) 1.46 (89% $E'$ , 11% $E''$ )

TABLE III. Results for the  $\text{Cu}^{2+} 3d^9$  multiplet structure (relative energies in eV) using the idealized lattice configuration proposed in Ref. [7]. The MRCI values include Davidson corrections [32]. The character of the SO wave-functions is also provided.

$3d^9$ states	CASSCF	MRCI	SO-MRCI
${}^2A'_1$	0	0	0 (99% $A'_1$ character)
${}^2E'$	0.98	1.17	1.08 (99% $E'$ ) 1.12 (72% $E''$ , 28% $E'$ )
${}^2E''$	1.03	1.22	1.30 (99% $E''$ ) 1.34 (72% $E'$ , 28% $E''$ )

in Table II (1.20 and 1.30 eV) and neglecting second-order SO couplings, these first-order splittings translate into excitation energies of 1.15, 1.25 eV ( $E''$  terms) and 1.20, 1.40 eV ( $E'$  terms) for the SO excited states, different from the results of the full SO-MRCI computation (1.12, 1.21, 1.28, and 1.46 eV). Compared to earlier calculations based on the angular overlap model (AOM) [7], our *ab initio* quantum chemical results differ therefore in two aspects: a different sequence of the  $E'$  and  $E''$  terms in the absence of first-order SO interactions ( $E(^2E') > E(^2E'')$  in Table II while  $E(^2E') < E(^2E'')$  in the AOM model [7]) and significantly stronger first-order SO interactions for the  $E''$  states (split in first order by 101 meV here, see above, and by 62 meV ( $500 \text{ cm}^{-1}$ ) in the AOM model [7]).

As concerns a direct comparison between the relative energies of the SO states with significant  $E'$  character listed in Table II and the positions of the peaks in the optical absorption spectrum [7], it is seen that the agreement is not perfect: 1.12, 1.21, and 1.46 eV vs 1.18, 1.35, and 1.60 eV (9500, 10900, and  $12900 \text{ cm}^{-1}$  in Ref. [7]). Deviations of  $\sim 0.1$  eV between MRCI excitation energies and experimental peak positions, with MRCI constantly underestimating experimental values, are however common for  $\text{Cu}^{2+} 3d^9$  oxide compounds [38, 39].

For completeness, we additionally provide in Table III on-site excitation energies computed on the basis of the more idealized crystal structure with identical  $\text{MO}_5$  cages. The crystal-field  $a'_1 - e'$  and  $a'_1 - e''$  splittings (which we denote as  $\delta'$  and  $\delta''$ , respectively) are different in this case, with  $\delta' < \delta''$ . A reversed sequence of the  $e'$  and  $e''$  levels in the two different crystal structures is also found by density-functional theory, by Wannier projection of the GGA bands onto the five  $3d$  orbitals at a Cu site, as discussed in Appendix. Most importantly, with SO couplings accounted for, the calculated excitation energies are far from the peak positions found in optics (see Table III). In particular, ‘pairs’ of nearly-degenerate SO states are obtained computationally for the more idealized crystal structure, different from the three-peak structure observed experimentally [7]. A more consistent picture in modeling experimental data was also found in the AOM frame [7] when elongated in-plane Cu-O bonds are employed.

## IV. Conclusions

In sum, a detailed analysis of the Cu  $d$ -shell electronic structure in the quasi-2D honeycomb compound  $\text{InCu}_{2/3}\text{V}_{1/3}\text{O}_3$  is performed, with focus on the interplay of electron correlations, spin-orbit couplings, and structural effects in this material. *Ab initio* computational data are compared to the outcome of ESR experiments and of previous optical absorption measurements [7]. The three-peak structure of the optical spectra is reproduced by many-body quantum chemical calculations only for atomic positions obtained from a prior lattice optimization relying on density-functional theory and not for a more idealized crystal structure with identical  $\text{MO}_5$  cages. It seems to be related with the fact that  $E'-E''$  mixing occurs for only two of the spin-orbit excited states. To describe electron correlation effects, we relied on multireference configuration-interaction calculations with single and double excitations out of the copper  $3d$  and oxygen  $2p$  shells within a given  $\text{CuO}_5$  unit. Although the correlation-induced corrections obtained this way to the  $d-d$  excitation energies are sizable, 0.1–0.2 eV, deviations in the range of 0.1 eV still remain as compared to experimental peak positions. On the other hand, the computed ground-state  $g$  factors are in excellent agreement with values derived from all available ESR data, within 98–99%. The peculiar coordination generates strong axial anisotropy at copper sites in  $\text{InCu}_{2/3}\text{V}_{1/3}\text{O}_3$ , reminiscent to some extent of, e.g., linearly coordinated transition-metal ions [1, 2, 18–20]. Adjusting the sequence of crystal-field levels through adequate design of the chemical/electrostatic environment [36, 40] such that the  $z^2$  orbital is filled leaves room for interesting single-ion magnetic properties even for the  $3d^9$  electron configuration, as pointed out in Refs. [19, 20].

### Acknowledgements

We thank A. Jesche for useful discussions, U. Nitzsche for technical assistance, and A. Möller for providing a sample of  $\text{InCu}_{2/3}\text{V}_{1/3}\text{O}_3$  for the ESR experiment and for important comments to the manuscript. L.H. acknowledges financial support from the German Research Foundation (Deutsche Forschungsgemeinschaft, DFG), grant HO-4427/3. O.J. was supported by the Leibniz Association through the Leibniz Competition.

### A. Computational details

To evaluate crystal-field parameters and the SO coupling constant  $\zeta$  within the GGA, we performed Wannier projections of the GGA bands onto the five  $3d$  orbitals at a Cu site. As these orbitals hybridize with oxygen  $2p$  and vanadium  $3d$  orbitals, the resulting hoppings sensibly depend on the energy window used for projections. Moreover, the Fourier-transformed Wannier func-

TABLE IV. Eigenvalues  $\lambda_n$  of the local Hamiltonian  $H_0$  parameterized using Wannier projection. In the fully relativistic calculations (GGA+SOC), all eigenvalues are doubly degenerate. All values are given in eV with respect to the Fermi level.

Eigenvalues of $H_0$	Identical $\text{O}_5$ cages		Optimized O positions	
	GGA	GGA+SOC	GGA	GGA+SOC
$\lambda_1$	-1.61	-1.65	-1.44	-1.48
$\lambda_2$	-1.60	-1.60	-1.43	-1.46
$\lambda_3$	-1.31	-1.37	-1.25	-1.29
$\lambda_4$	-1.31	-1.24	-1.25	-1.17
$\lambda_5$	-0.26	-0.26	-0.15	-0.15

tions show deviations from the GGA bands at the bottom of the valence band, especially for the experimental structure. However, we are interested exclusively in the local terms, and these show only a small (on the order of several meV) dependence on the energy window. Using parameters obtained from such a procedure, we construct the local Hamiltonian  $H_0$ . Corresponding eigenvalues are provided for both crystal structures in Table IV.

For both lattice configurations,  $H_0$  features two pairs of nearly degenerate eigenstates:  $\lambda_1 \simeq \lambda_2$  and  $\lambda_3 \simeq \lambda_4$ . But the gaps between them,  $\Delta_1 = \lambda_3 - \lambda_2$  and  $\Delta_2 = \lambda_5 - \lambda_4$ , differ significantly in  $\text{InCu}_{2/3}\text{V}_{1/3}\text{O}_3$ :  $\Delta_1 \simeq 0.30$  (0.19) eV is substantially smaller than  $\Delta_2 \simeq 1.06$  (1.10) eV in the idealized (optimized) structure. As concerns the sequence of the two groups of nearly degenerate states, we found that in the more idealized crystal structure  $\lambda_1$  has dominant (84%)  $xz$  character while  $\lambda_2$  is dominated (84%) by the  $yz$  orbital. Similarly,  $\lambda_3$  and  $\lambda_4$  pertain to the  $xy$  and  $x^2 - y^2$  orbitals, respectively. But in the optimized structure, the order is reversed: the lower-lying eigenstates in each group,  $\lambda_1$  and  $\lambda_3$ , are dominated by  $yz$  (94%) and  $x^2 - y^2$  (61%) orbitals.

Finally, we applied a fully relativistic GGA treatment and performed Wannier projections to estimate the SO coupling constant  $\zeta$ . The respective eigenvalues are provided in Table IV next to those for the scalar-relativistic case [41]. The SO coupling  $\zeta$  can be then estimated by averaging over two offdiagonal elements of  $H_0$ :

$$\zeta = -\frac{1}{2\sqrt{3}} \left( i \langle \phi_{z^2}^\uparrow | H_0 | \phi_{yz}^\downarrow \rangle + \langle \phi_{z^2}^\uparrow | H_0 | \phi_{xz}^\downarrow \rangle \right), \quad (\text{A1})$$

where  $\phi_\alpha^\sigma$  is the basis (Wannier) function of orbital  $\alpha$  and spin  $\sigma$ . We obtain this way  $\zeta = 68$  (60) meV for the idealized (optimized) structure.

As concerns the quantum chemical calculations, the actual cluster considered in the computations consists of a central  $\text{CuO}_5$  unit along with three adjacent  $\text{VO}_5$  polyhedra, three Cu nearest neighbors, and six adjacent In ions. The remaining part of the extended crystalline surroundings was modeled as an effective electrostatic field [42]. For the central  $\text{CuO}_5$  unit, all-electron Douglas-Kroll basis sets of triple- $\zeta$  quality with polarization functions were used. For farther oxygen ligands in the cluster and for the nearby V ions, we applied basis sets of

double- $\zeta$  quality. The results discussed in the main text were obtained by modeling the  $\text{Cu}^{2+}$  nearest neighbors as closed-shell  $\text{Zn}^{2+}$  total-ion potentials (TIP's), an approximation also employed in earlier quantum chemical investigations [38, 39, 43]. Test CASSCF calculations in which the three adjacent Cu species are represented

as  $2+ S = 1/2 3d^9$  ions provide central-site crystal-field splittings that agree within 0.01 eV with those computed with  $\text{Zn}^{2+}$  TIP's. We used the latter for all subsequent computations since this makes the spin-orbit calculations and related analysis much less complex. TIP's were also applied for the nearby  $\text{In}^{3+}$  ions.

- 
- <sup>1</sup> J. M. Zadrozny, D. J. Xiao, M. Atanasov, G. J. Long, F. Grandjean, F. Neese, and J. R. Long, *Nat. Chem.* **5**, 577 (2013).
- <sup>2</sup> A. Jesche, R. W. McCallum, S. Thimmaiah, J. L. Jacobs, V. Taufour, A. Kreyssig, R. S. Houk, S. L. Bud'ko, and P. C. Canfield, *Nat. Commun.* **5**, 3333 (2014).
- <sup>3</sup> D. Li, K. Lee, B. Y. Wang, M. Osada, S. Crossley, H. R. Lee, Y. Cui, Y. Hikita, and H. Y. Hwang, *Nature* **572**, 624 (2019).
- <sup>4</sup> M. Hepting, D. Li, C. J. Jia, H. Lu, E. Paris, Y. Tseng, X. Feng, M. Osada, E. Been, Y. Hikita, Y.-D. Chuang, Z. Hussain, K. J. Zhou, A. Nag, M. Garcia-Fernandez, M. Rossi, H. Y. Huang, D. J. Huang, Z. X. Shen, T. Schmitt, H. Y. Hwang, B. Moritz, J. Zaanen, T. P. Devereaux, and W. S. Lee, *Nat. Mater.* **19**, 381 (2020).
- <sup>5</sup> M. Jiang, M. Berciu, and G. A. Sawatzky, *Phys. Rev. Lett.* **124**, 207004 (2020).
- <sup>6</sup> V. Kataev, A. Möller, U. Löw, W. Jung, N. Schittner, M. Kriener, and A. Freimuth, *J. Magn. Magn. Mater.* **290-291**, 310 (2004).
- <sup>7</sup> A. Möller, U. Löw, T. Taetz, M. Kriener, G. André, F. Damay, O. Heyer, M. Braden, and J. A. Mydosh, *Phys. Rev. B* **78**, 024420 (2008).
- <sup>8</sup> M. Yehia, E. Vavilova, A. Möller, T. Taetz, U. Löw, R. Klingeler, V. Kataev, and B. Büchner, *Phys. Rev. B* **81**, 060414 (2010).
- <sup>9</sup> S. Okubo, H. Wada, H. Ohta, T. Tomita, M. Fujisawa, T. Sakurai, E. Ohmichi, and H. Kikuchi, *J. Phys. Soc. Jpn.* **80**, 023705 (2011).
- <sup>10</sup> Y. J. Yan, Z. Y. Li, T. Zhang, X. G. Luo, G. J. Ye, Z. J. Xiang, P. Cheng, L. J. Zou, and X. H. Chen, *Phys. Rev. B* **85**, 085102 (2012).
- <sup>11</sup> S.-Q. Jia, Q.-W. Wang, J. Liu, and L.-J. Zou, *J. Phys.: Conf. Ser.* **827**, 012010 (2017).
- <sup>12</sup> S.-Q. Jia, Q.-W. Wang, X.-L. Yu, and L.-J. Zou, *AIP Advances* **7**, 055825 (2017).
- <sup>13</sup> M. Iakovleva, O. Janson, H.-J. Grafe, A. P. Dioguardi, H. Maeter, N. Yeche, H.-H. Klauss, G. Pascua, H. Luetkens, A. Möller, B. Büchner, V. Kataev, and E. Vavilova, *Phys. Rev. B* **100**, 144442 (2019).
- <sup>14</sup> V. L. Berezinskii, *Sov. Phys JETP-USSR* **32**, 493 (1971).
- <sup>15</sup> J. M. Kosterlitz and D. J. Thouless, *J. Phys. C: Solid State Phys.* **5**, L124 (1972).
- <sup>16</sup> J. M. Kosterlitz and D. J. Thouless, *J. Phys. C: Solid State Phys.* **6**, 1181 (1973).
- <sup>17</sup> J. M. Kosterlitz, *J. Phys. C: Solid State Phys.* **7**, 1046 (1974).
- <sup>18</sup> L. Xu, Z. Zangeneh, R. Yadav, S. Avdoshenko, J. van den Brink, A. Jesche, and L. Hozoi, *Nanoscale* **9**, 10596 (2017).
- <sup>19</sup> A. Jesche, L. Ke, J. L. Jacobs, B. Harmon, R. S. Houk, and P. C. Canfield, *Phys. Rev. B* **91**, 180403 (2015).
- <sup>20</sup> V. P. Antropov and V. N. Antonov, *Phys. Rev. B* **90**, 094406 (2014).
- <sup>21</sup> J. L. Lado and V. Pardo, *Phys. Rev. B* **94**, 115141 (2016).
- <sup>22</sup> R. Kubo and K. Tomita, *J. Phys. Soc. Jpn.* **9**, 888 (1954).
- <sup>23</sup> D. L. Huber, *Phys. Rev. B* **6**, 3180 (1972).
- <sup>24</sup> P. M. Richards and M. B. Salamon, *Phys. Rev. B* **9**, 32 (1974).
- <sup>25</sup> H. Benner and J. Boucher, in *Magnetic Properties of Layered Transition Metal Compounds*, edited by L. de Jongh (Kluwer Academic Publishers, Dordrecht, 1990) Chap. Spin Dynamics in the Paramagnetic Regime: NMR and EPR in Two-Dimensional Magnets, pp. 323–378.
- <sup>26</sup> J. Zeisner, A. Alfonsov, S. Selter, S. Aswartham, M. P. Ghimire, M. Richter, J. van den Brink, B. Büchner, and V. Kataev, *Phys. Rev. B* **99**, 165109 (2019).
- <sup>27</sup> K. Koepernik and H. Eschrig, *Phys. Rev. B* **59**, 1743 (1999).
- <sup>28</sup> J. P. Perdew, K. Burke, and M. Ernzerhof, *Phys. Rev. Lett.* **77**, 3865 (1996).
- <sup>29</sup> A. I. Lichtenstein and M. I. Katsnelson, *Phys. Rev. B* **57**, 6884 (1998).
- <sup>30</sup> N. Ahmed, A. A. Tsirlin, and R. Nath, *Phys. Rev. B* **91**, 214413 (2015).
- <sup>31</sup> K. Nawa, O. Janson, and Z. Hiroi, *Phys. Rev. B* **96**, 104429 (2017).
- <sup>32</sup> T. Helgaker, P. Jørgensen, and J. Olsen, *Molecular Electronic-Structure Theory* (Wiley, Chichester, 2000).
- <sup>33</sup> H. J. Werner, P. J. Knowles, G. Knizia, F. R. Manby, and M. Schütz, *Wiley Rev: Comp. Mol. Sci.* **2**, 242 (2012).
- <sup>34</sup> A. Berning, M. Schweizer, H.-J. Werner, P. J. Knowles, and P. Palmieri, *Mol. Phys.* **98**, 1823 (2000).
- <sup>35</sup> However, for the  $3d^9$  manifold and sufficiently high symmetry, this essentially corresponds to single-configuration restricted open-shell Hartree-Fock (ROHF) [32].
- <sup>36</sup> N. A. Bogdanov, V. M. Katukuri, J. Romhányi, V. Yushankhai, V. Kataev, B. Büchner, J. van den Brink, and L. Hozoi, *Nat. Commun.* **6**, 7306 (2015).
- <sup>37</sup> P. J. Knowles and H.-J. Werner, *Theor. Chim. Acta* **84**, 95 (1992).
- <sup>38</sup> L. Hozoi, L. Siurakshina, P. Fulde, and J. van den Brink, *Sci. Rep.* **1**, 65 (2011).
- <sup>39</sup> H.-Y. Huang, N. A. Bogdanov, L. Siurakshina, P. Fulde, J. van den Brink, and L. Hozoi, *Phys. Rev. B* **84**, 235125 (2011).
- <sup>40</sup> Z. Zangeneh, S. Avdoshenko, J. van den Brink, and L. Hozoi, *Phys. Rev. B* **100**, 174436 (2019).
- <sup>41</sup> Note that the fully relativistic calculations are nonmagnetic and all eigenvalues are doubly degenerate.
- <sup>42</sup> M. Klintonberg, S. E. Derenzo, and M. J. Weber, *Comput. Phys. Commun.* **131**, 120 (2000).
- <sup>43</sup> N. A. Bogdanov, V. Bisogni, R. Kraus, C. Monney, K. Zhou, T. Schmitt, J. Geck, A. O. Mitrushchenkov, H. Stoll, J. van den Brink, and L. Hozoi, *J. Phys. Condens. Matter* **29**, 035502 (2017).